CMS Physics Analysis Summary

Contact: cms-pag-conveners-exotica@cern.ch 2018/03/12

Search for pair production of second generation leptoquarks at $\sqrt{s} = 13$ TeV

The CMS Collaboration

Abstract

A search for pair production of second-generation leptoquarks is performed using 35.9 fb^{-1} of data collected at $\sqrt{s} = 13$ TeV in 2016 with the CMS detector at the CERN LHC. Final states with two muons and two jets, or with one muon, two jets, and missing transverse energy are considered. Second-generation leptoquarks with masses less than 1530 GeV (1285 GeV) are excluded for β=1.0 (0.5), where β is the branching fraction of a leptoquark decaying to a charged lepton and a quark. These limits are the most stringent to date on the masses of second-generation leptoquarks. The results of the search are reinterpreted within a long-lived R-parity violating supersymmetry model that also has a final state with two muons and two jets.

1 Introduction

Leptoquarks (LQs) are new bosons predicted by numerous extensions of the standard model (SM) such as GUTs, composite models with lepton and quark substructure, technicolor, and superstring-inspired models [1–13]. They are color-triplet scalar or vector bosons carrying both lepton and baryon number, and decay to a lepton and a quark.

LQs have recently attracted increased interest as a possible explanation for the observation of anomalies in B meson decays by the Belle [14–16], BABAR [17, 18], and LHCb [19–21] Collaborations.

The dominant leading-order processes for the pair production of scalar leptoquarks at the LHC involve gluon-gluon fusion. Quark-antiquark scattering and annihilation also contribute, to a lesser degree. Both sets of processes are shown in Fig. 1.

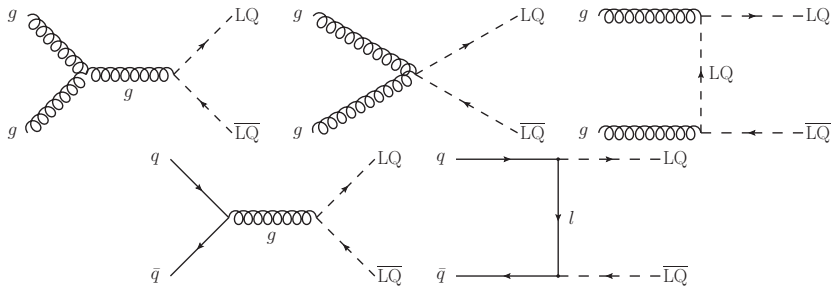

Figure 1: Dominant leading-order diagrams for the pair production of scalar leptoquarks.

The rates of LQ production and decay depend on two model parameters: the Yukawa coupling at the LQ-lepton-quark vertex λ_{LQ}, and the branching fraction of the LQ decay to a charged lepton and a quark, β. The decay of the LQ to a neutrino and quark is complementary to the charged lepton quark decay and has branching fraction 1-β. In this analysis the LQ decays are assumed to be prompt and therefore the pair production cross sections and limits are not dependent on λ_{LQ}. Values of 1 and 0.5 are considered for β, leading to the two final states $\mu\mu$jj and $\mu\nu$jj.

Other models of physics beyond the SM, such as R-parity violating (RPV) supersymmetry (SUSY) [22], also give rise to LQ-like phenomenology. SUSY postulates a symmetry between fermions and bosons, which gives rise to superpartner particles for all known SM particles. In some SUSY scenarios, top quark super-partners (top squark, $\widetilde{\mathrm{t}}$) are the lightest supersymmetric particles and can decay to a b quark and a charged lepton when R-parity is violated. For $\widetilde{\mathrm{t}}$ pair production and direct $\widetilde{\mathrm{t}}$ to charged lepton + b quark decays, limits can be extracted directly from LQ limits. If the couplings of the RPV operators are sufficiently small, however, the superpartners will have a non-zero lifetime, and will travel through part or all of the detector before decaying. In this scenario, referred to in this paper as displaced SUSY [23], the $\widetilde{\mathrm{t}}$ has a finite but non-zero lifetime, and decays to a charged lepton and a b quark after a distance, $c\tau$, between 0.1 and 100 cm. This analysis can provide sensitivity in a phase space complementary to that of dedicated searches for displaced SUSY, particularly in the low-lifetime, high-mass regime where dedicated searches lose sensitivity.

2 The CMS detector

The central feature of the CMS apparatus is a superconducting solenoid of 6 m internal diameter, providing a magnetic field of 3.8 T. Within the solenoid volume are a silicon pixel and strip

tracker, a lead tungstate crystal electromagnetic calorimeter, and a brass and scintillator hadron calorimeter (HCAL), each composed of a barrel and two endcap sections. Forward calorimeters extend the pseudorapidity coverage provided by the barrel and endcap detectors. Muons are measured in gas-ionization detectors embedded in the steel flux-return yoke outside the solenoid. A more detailed description of the CMS detector, together with a definition of the coordinate system used and the relevant kinematic variables, can be found in Ref. [24].

3 Data and simulation samples

The data set used in this paper was collected by CMS during the 2016 LHC run and corresponds to an integrated luminosity of $35.9 \pm 0.9\,\text{fb}^{-1}$. The luminosity measurement is described in Ref. [25].

Events are selected using a trigger path that requires at least one muon with p_T greater than 50 GeV, with no isolation requirements. This trigger path supplies the data for the $\mu\mu$jj and $\mu\nu$jj channels, as well as for the eμ sample used in the $\text{t}\bar{\text{t}}$ +jets background estimate in the $\mu\mu$jj channel.

Signal and background events are generated using the NNPDF3.0 parton distribution function (PDF) sets [26], and simulated with the full detector geometry using GEANT4 [27, 28].

Signal samples are produced in 50 GeV steps for scalar LQ masses between 200 and 2000 GeV at leading order (LO) with PYTHIA8 [29, 30]. These samples are normalized to next-to-leading-order (NLO) production cross sections using, the CTEQ6L1 PDF set [31], for comparison with data. The search limits are independent of λ_{LQ}, which has been set to $\lambda_{EM} = 0.3$ in the signal simulation. Displaced SUSY samples are produced for $\widetilde{\text{t}}$ masses from 200 to 1200 GeV, with 100 GeV steps, for $c\tau = 0.1$, 1, 10, and 100 cm, also with PYTHIA8 and NNPDF3.0. Production cross sections for $\widetilde{\text{t}}$ are calculated at the NLO + next-to-leading-logarithm (NLL) level using PROSPINO [32] and the NLL-FAST program [33, 34], using the CTEQ6L1 PDF set.

Standard model backgrounds considered include Z/γ^*+jets, $\text{t}\bar{\text{t}}$ +jets, W+jets, single top quark production, and diboson (WW/WZ/ZZ)+jets. The Z/γ^*+jets, W+jets, and diboson samples are generated at NLO using MADGRAPH5_AMC@NLO [35, 36]. Single top quark and $\text{t}\bar{\text{t}}$ +jets samples are generated at NLO using POWHEG V2 [37–39] and MADGRAPH5_AMC@NLO.

The W+jets and Z/γ^*+jets samples are normalized to next-to-next-to-leading-order (NNLO) inclusive cross sections calculated with FEWZ version 3.1 and 3.1.b2, respectively [40]. Single top quark and diboson samples are normalized to NLO inclusive cross sections calculated with MCFM version 6.6 [41–44]. The $\text{t}\bar{\text{t}}$ sample is normalized to calculations at the NNLO + next-to-NLL level [45, 46].

The simulated samples are corrected so that the detector response and resolution for both leptons and jets and the triggering efficiency match those found in data.

4 Event reconstruction and selection

The particle-flow event algorithm which reconstructs and identifies each individual particle with an optimized combination of information from the various elements of the CMS detector [47].

The reconstructed vertex with the largest value of summed physics-object p_T^2 is taken to be the primary pp interaction vertex. The physics objects are the jets, clustered using the jet finding

algorithm [48, 49] with the tracks assigned to the vertex as inputs, and the associated missing transverse momentum, taken as the negative vector sum of the p_T of those jets. The missing transverse energy (E_T^{miss}) is defined as the magnitude of the missing transverse momentum vector. Jet energy corrections are propagated to the E_T^{miss}.

Jets are reconstructed offline using the anti-k_t algorithm [48, 49] with a size parameter of 0.4. Jet momentum is determined as the vectorial sum of all particle momenta in the jet, and is found from simulation to be within 5 to 10% of the true momentum over the whole p_T spectrum and detector acceptance. Additional proton-proton interactions within the same or nearby bunch crossings can contribute additional tracks and calorimetric energy depositions to the jet momentum. To mitigate this effect, tracks identified to be originating from pileup vertices are discarded, and an offset correction is applied to correct for remaining contributions. Jet energy corrections are derived from simulation to bring measured response of jets to that of particle level jets on average. In situ measurements of the momentum balance in dijet, photon + jet, Z+jet, and multijet events are used to account for any residual differences in jet energy scale in data and simulation. Additional selection criteria are applied to each jet to remove jets potentially dominated by anomalous contributions from various subdetector components or reconstruction failures. Jets are required to have pseudorapidity $|\eta| < 2.4$, $p_T > 50\,\text{GeV}$, and to be separated from all slected muons by $\Delta R = 0.5$.

Muons are measured in the pseudorapidity range $|\eta| < 2.4$, with detection planes made using three technologies: drift tubes, cathode strip chambers, and resistive plate chambers. Muons are reconstructed as tracks combining hit segments in the muon system and hits in the inner tracking system. Matching muons to tracks measured in the silicon tracker results in a relative transverse momentum resolution for muons with $20 < p_T < 100\,\text{GeV}$ of 1.3–2.0% in the barrel and better than 6% in the endcaps. The p_T resolution in the barrel is better than 10% for muons with p_T up to 1 TeV [50]. Muons are required to have $p_T > 53$ GeV and $|\eta| < 2.4$, and are required to satisfy a set of identification criteria optimized for high p_T. They require at least one muon detector segment be included in the muon track fit, and segments in at least two muon stations be geometrically matched to a track in the inner tracking system. An isolation requirement is imposed to select high-quality muons. The sum of the transverse momenta of all tracks in the tracker originating from the primary vertex in a cone of $\Delta R = \sqrt{\Delta\phi^2 + \Delta\eta^2} = 0.3$ around the muon track (excluding the muon track itself), divided by the muon p_T, is less than 0.1. In order to suppress muons from decays in flight and to allow a more precise p_T measurement, at least 8 tracker layers with hits associated to the muon are required, and at least one hit in the pixel detector. To reject muons from cosmic rays, the transverse impact parameter of the muon track from the primary vertex is required to be less than 2 mm and the longitudinal distance of the track with respect to the primary vertex is required to be less than 5 mm.

The electron momentum is estimated by combining the energy measurement in the ECAL with the momentum measurement in the tracker. The momentum resolution for electrons with $p_T \approx 45\,\text{GeV}$ from $Z \to ee$ decays ranges from 1.7% for nonshowering electrons in the barrel region to 4.5% for showering electrons in the endcaps [51].

The LQ candidates are reconstructed in the $\mu\mu$jj channel by pairing each muon with a jet in the configuration that minimizes the LQ-$\overline{\text{LQ}}$ invariant mass difference. In the $\mu\nu$jj channel the muon and E_T^{miss} are each paired with a jet in a similar manner using the invariant mass and transverse mass, respectively.

5 Estimation of standard model backgrounds

5.1 The $\mu\mu$jj channel

The main backgrounds which can mimic LQ signal in the $\mu\mu$jj channel are Z/γ^*+jets and $t\bar{t}$ +jets events.

The Z/γ^*+jets background is estimated using a simulated sample normalized to a disjoint data control region. The background shape is taken from simulation, and a data normalization scale factor is determined using a $80 < M_{\mu\mu} < 100\,\text{GeV}$ window. This scale factor is 0.98 ± 0.01 (stat)±0.09 (syst).

The $t\bar{t}$ background is estimated using an orthogonal eμ data sample. Events are selected containing one electron and one muon. This sample is corrected for differences between $\mu\mu$ and eμ selection such as electron and muon identification and isolation, as well as trigger efficiency. The kinematic distributions of this sample are found to be in good agreement with $t\bar{t}$ simulation, while reducing the systematic uncertainties associated with this background.

Backgrounds from single top, W+jets, and diboson events are estimated from simulation. Background from QCD multijets is shown to be negligible and is not considered.

Backgrounds are compared to a data sample with looser selection criteria. This preselection requires at least two muons with $p_T > 53\,\text{GeV}$ and at least two jets with $p_T > 50\,\text{GeV}$. The muons are required to be separated from one another by $\Delta R > 0.3$. The invariant mass of the di-muon system ($M_{\mu\mu}$) is required to be greater than 50 GeV, and the $S_T^{\mu\mu jj}$ of the event is required to be greater than 300 GeV, where $S_T^{\mu\mu jj}$ is defined as the scalar sum of the transverse momenta of the two jets and two muons in the event.

After preselection, three kinematic variables are used to define a set of final cuts for each LQ mass. In the $\mu\mu$jj channel, the optimization variables are $S_T^{\mu\mu jj}$, $M_{\mu\mu}$, and $M_{\mu j}^{min}$, where $M_{\mu j}^{min}$is defined as the smaller of the two muon-jet invariant masses that minimize the LQ-$\overline{LQ}$ invariant mass difference. A comparison of these main kinematic variables is shown at preselection level in Fig. 2. A full three-dimensional optimization is performed, with signal-to-background separation optimized using the Punzi significance [52], which is optimal for both setting limits and for making a discovery, and is valid in cases with low background statistics.

5.2 The $\mu\nu$jj channel

A background-dominated preselection is used to estimate and validate standard model backgrounds. This preselection requires exactly one muon with $p_T > 53\,\text{GeV}$ and at least two jets with $p_T > 50\,\text{GeV}$. The muon in the event is required to be separated from the E_T^{miss} by $\Delta\phi > 0.8$, and the leading jet in the event is required to be separated from the E_T^{miss} by $\Delta\phi > 0.8$. The $M_T^{\mu\nu}$ of the event is required to be greater than 50 GeV. The E_T^{miss} of the event is required to be greater than 55 GeV, and the $S_T^{\mu\nu jj}$ of the event is required to be greater than 300 GeV, where $S_T^{\mu\nu jj}$ is defined as the scalar sum of the transverse momenta of the two jets, the muon, and the E_T^{miss} in the event.

The main backgrounds, which can mimic the LQ signal in the $\mu\nu$jj channel, are W+jets and $t\bar{t}$ +jets events. W+jets and $t\bar{t}$ backgrounds are both estimated using simulated samples normalized to disjoint data control regions. Both backgrounds are estimated at preselection in a $70 < M_T^{\mu\nu} < 110$ window. Then b-tagging [53] information is used to produce disjoint control regions and to further enrich the samples with their respective background processes. The W+jets background control region requires exactly 0 b-tagged jets, while the $t\bar{t}$ control sample

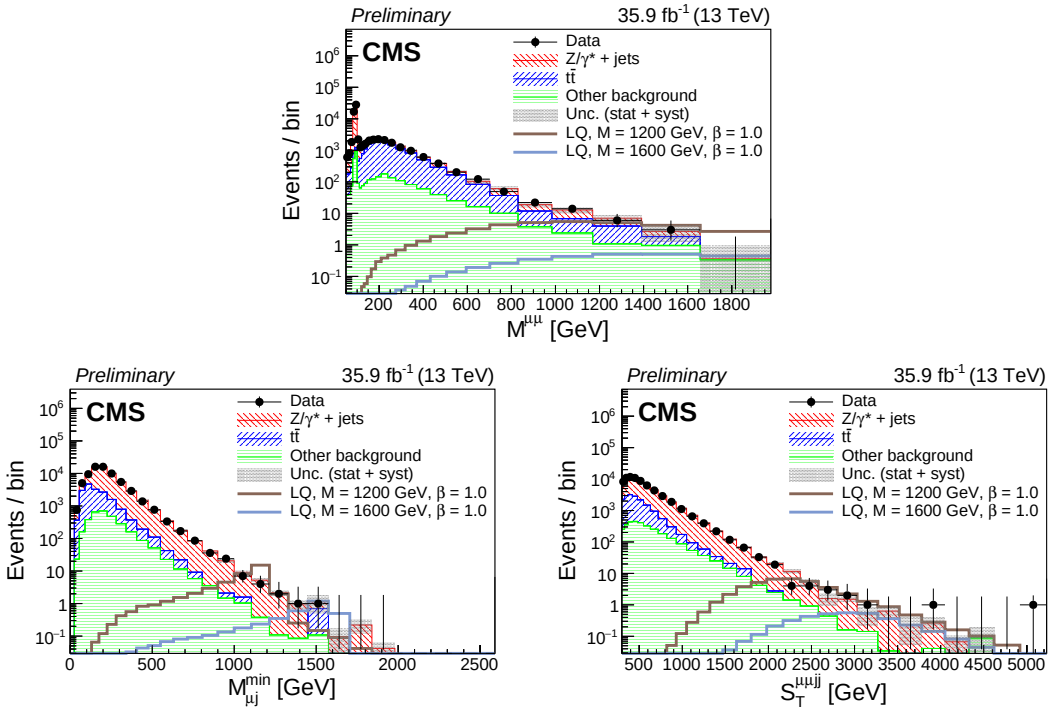

Figure 2: Data and background comparison at preselection level for the $\mu\mu$jj channel, shown for the variables used for final selection cut optimization $M_{\mu\mu}$ (top), $M^{\text{min}}_{\mu j}$ (bottom left), and $S_T^{\mu\mu jj}$ (bottom right).

requires at least one b-tagged jet. The W+jets data normalization scale factor is found to be 0.93±0.01 (stat), and the $t\bar{t}$ data normalization scale factor is found to be 0.98±0.01 (stat).

Backgrounds from single top, Z/γ^*+jets, and diboson events are estimated from simulation. Backgrounds from QCD multijets are shown to be negligible and are not considered.

A comparison of the main kinematic variables used in the analysis is shown at preselection level in Fig. 3.

After preselection, a set of final cuts is defined for each LQ mass as for the $\mu\mu$jj channel. In the $\mu\nu$jj channel, the optimization variables are $S_T^{\mu\nu jj}$, $M_T^{\mu\nu}$, and $M_{\mu j}$, where $M_T^{\mu\nu}$ and $M_{\mu j}$ are defined as the muon-E_T^{miss} transverse mass and the muon-jet invariant mass which minimizes the LQ-$\overline{\text{LQ}}$ mass difference. The final selection cuts for the three variables for both channels are shown as a function of LQ mass in Figure 4.

6 Results

6.1 Final selection data comparison

The data are compared to background predictions after the final selections have been applied. Comparisons of background, data, and signal can be seen in Figs. 5 and 6. In these plots the final event counts in background, data, and signal are shown for each final selection. In these plots all bins are correlated, as each final selection for increasing LQ mass is a strict subset of the previous LQ mass selection. Kinematic comparisons after the final selection are shown for some LQ mass hypotheses for both channels in Fig. 7. No significant excess is seen for any

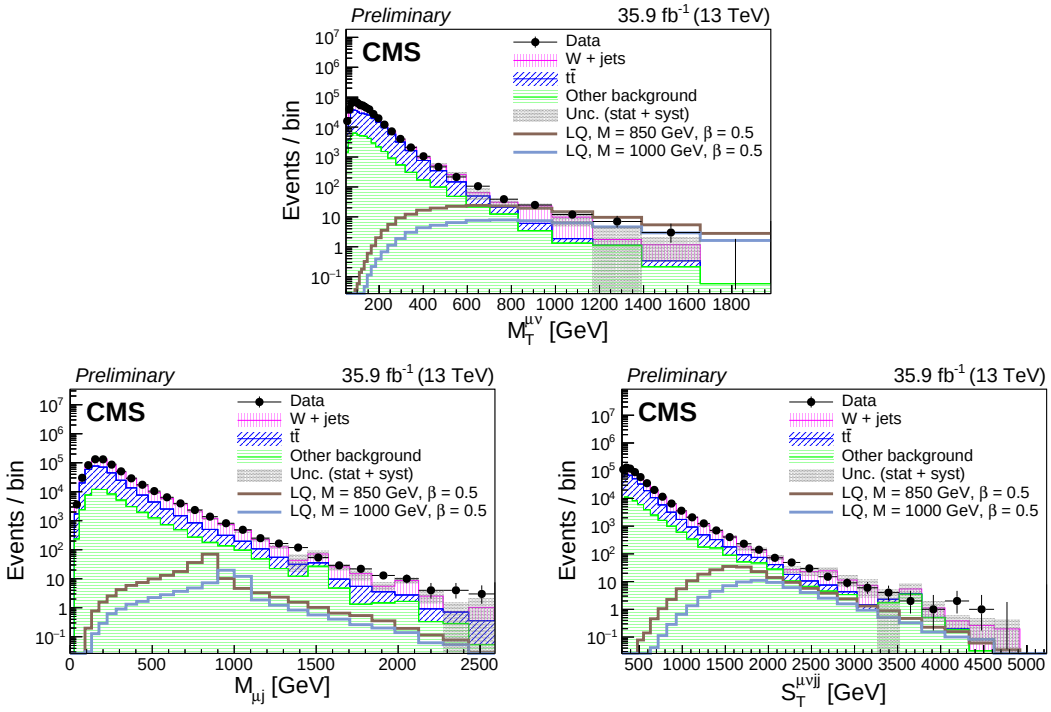

Figure 3: Data and background comparison at preselection level for the $\mu\nu$jj channel, shown for the variables used for final selection cut optimization $M_T^{\mu\nu}$ (top), $M_{\mu j}$ (bottom left), and $S_T^{\mu\nu jj}$ (bottom right).

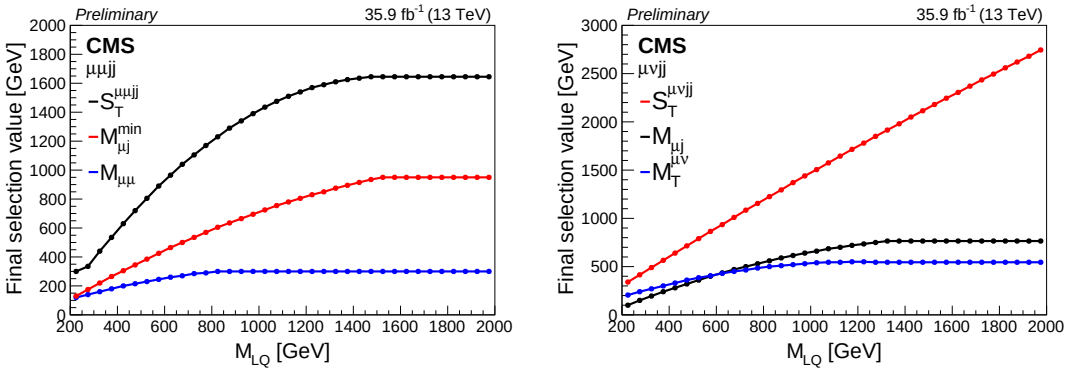

Figure 4: Final selection cuts for the three variables for both the $\mu\mu$jj (left) and $\mu\nu$jj (right) channels as a function of LQ mass.

LQ mass. A detailed table of the event counts in data, background, and signal is shown in Appendix B.

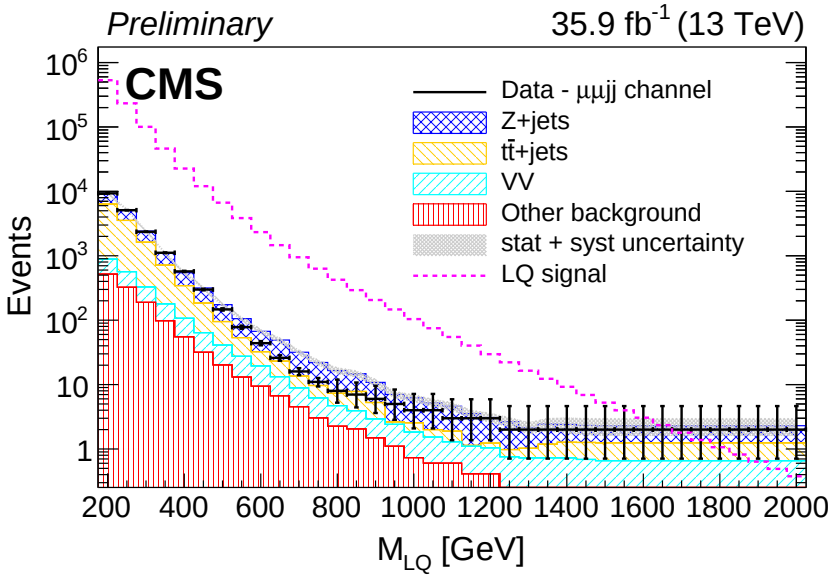

Figure 5: Data and background event yields at final selection level for the $\mu\mu jj$ analysis, as a function of leptoquark mass. 'Other background' includes W+jets and single top. The samples in individual bins are largely overlapping.

6.2 Systematic uncertainties

Systematic uncertainties in the background yields and in the signal acceptance for both the $\mu\mu$jj and $\mu\nu$jj channels are calculated for each final selection by running the full analysis with varied detector quantities, particle momenta, or scale factors. These yields are compared to those for the nominal analysis, and the differences are propagated as log-normal nuisance parameters in the limit setting. Systematic uncertainties in the jet energy resolution and muon energy resolution are measured by smearing the jet and muon momenta, including high-p_T specific corrections for muons. Uncertainties due to the jet energy scale and muon energy scale are measured by propagating jet and muon energy corrections. Other sources of systematic uncertainty considered are: the luminosity measurement, the muon and electron identification and isolation, the choice of PDF, pileup, the trigger efficiency, track reconstruction, $t\bar{t}$ shape and normalization, DY/γ^*+jets shape and normalization, W+jets shape and normalization, diboson shape, and b-tagging efficiency. The effects of these systematic uncertainties on signal acceptance and background yield are shown for the $\mu\mu$jj and $\mu\nu$jj channels in Tables 1 and 2, respectively. For most values of M_{LQ} the systematic uncertainties are at the lower end of the range. The maximum values in given in Tables 1 and 2 are only relevant for large values of M_{LQ}, where the total uncertainty is dominated by the statistical uncertainty of the simulated background samples.

6.3 Limit setting

Limits are set on the LQ pair-production cross section as a function of LQ mass using the asymptotic CL_S modified frequentist approach [54, 55]. The systematic uncertainties listed above are introduced as nuisance parameters in the limit setting procedure using log-normal probability functions. Uncertainties of statistical nature are described with Γ distributions with

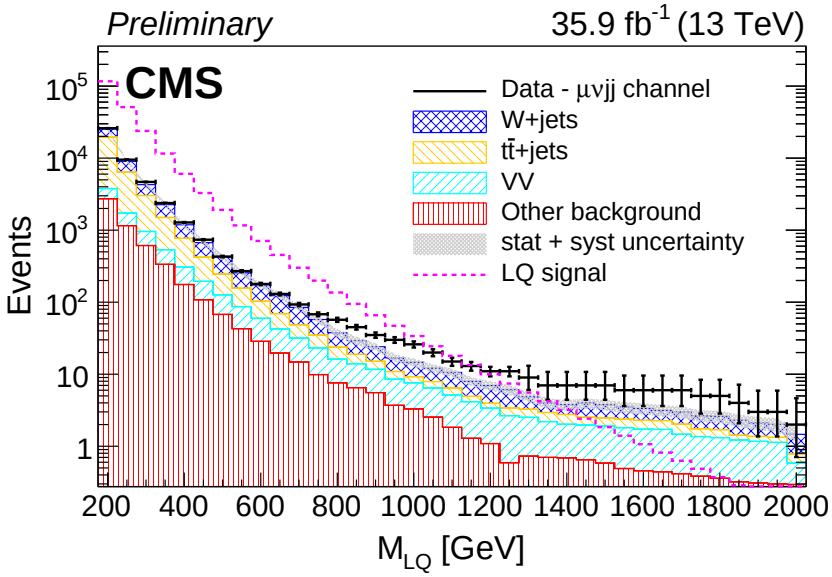

Figure 6: Data and background event yields at final selection level for the $\mu\nu jj$ analysis, as a function of leptoquark mass. 'Other background' includes Z+jets and single top. The samples in individual bins are largely overlapping.

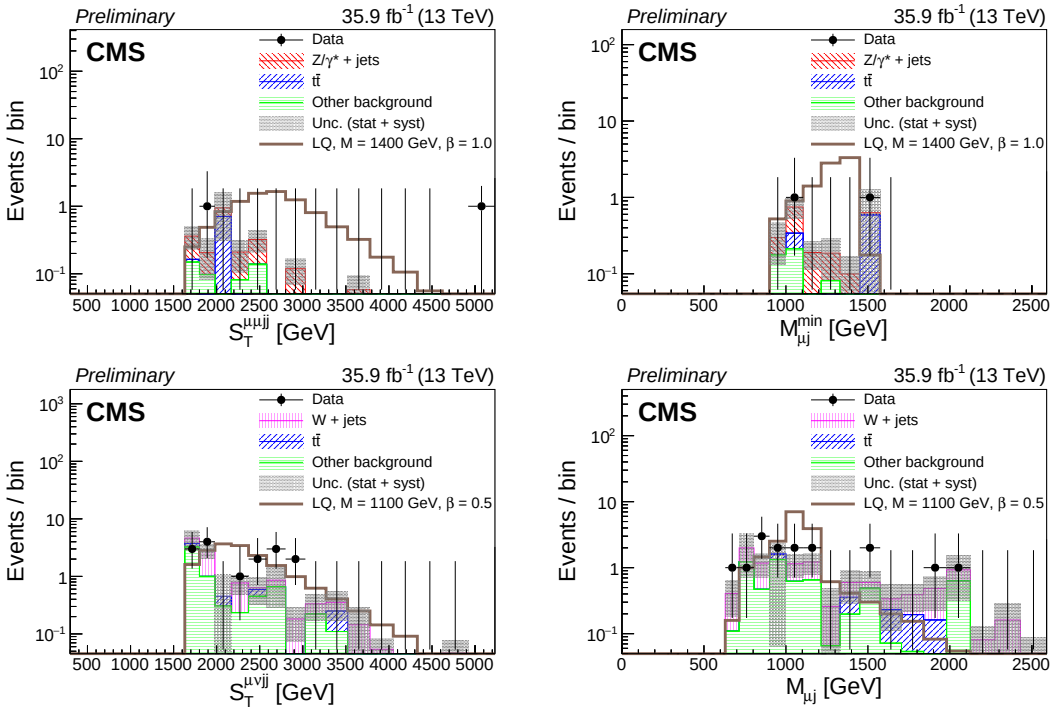

Figure 7: Data and background comparison at final selection level for $M_{LQ} = 1400\,\text{GeV}$ for the $\mu\mu$jj (top) and for $M_{LQ} = 1100$ for the $\mu\nu$jj (bottom) channel, shown for S_T (left) and LQ invariant mass (right).

$\mu\mu$jj uncertainty	Signal min - max (%)	BG min - max (%)
Jet energy resolution	0.02 - 0.43	0.28 - 4.78
Jet energy scale	0.1 - 1.81	0.42 - 4.92
Luminosity	2.5 - 2.5	0.27 - 0.92
Muon energy resolution	0.0 - 0.23	0.01 - 3.82
Muon energy scale	0.02 - 0.19	1.29 - 6.16
Muon ID/Isolation	6.11 - 6.75	1.15 - 2.92
PDF	1.88 - 3.96	0.39 - 4.59
PileUp	0.01 - 0.31	0.16 - 5.9
Trigger	0.14 - 0.73	0.03 - 0.46
Tracking efficiency	1.03 - 1.95	0.11 - 0.94
b-tagging efficiency	–	0.0 - 0.01
TT normalization	–	0.01 - 0.27
TT shape	–	0.01 - 0.01
W normalization	–	0.02 - 0.09
W shape	–	0.0 - 0.01
Z normalization	–	3.37 - 7.29
Z shape	–	1.48 - 6.2
Diboson shape	–	0.67 - 9.15
Total syst unc.	7.2 - 8.5	5.0 - 11.8
Total stat unc.	0.5 - 1.0	0.6 - 28.7

Table 1: Range of systematic uncertainties on the signal acceptance and background (BG) yields for the $\mu\mu$jj analysis. The last two lines show the total systematic uncertainty, and the total statistical uncertainty of the simulated samples, respectively.

$\mu\nu$jj uncertainty	Signal min - max (%)	BG min - max (%)
Jet energy resolution	1.24 - 2.33	3.4 - 6.07
Jet energy scale	0.01 - 0.75	0.73 - 6.73
Luminosity	2.5 - 2.5	0.47 - 1.39
Muon energy resolution	0.0 - 0.11	0.18 - 4.65
Muon energy scale	0.0 - 0.2	0.43 - 2.88
Muon ID/Isolation	2.98 - 3.1	0.54 - 2.54
PDF	0.35 - 0.83	0.91 - 5.56
PileUp	0.01 - 0.33	0.61 - 3.11
Trigger	4.19 - 7.47	0.78 - 5.46
Tracking efficiency	0.53 - 0.95	0.1 - 0.69
b-tagging efficiency	–	1.42 - 3.64
TT normalization	–	0.08 - 0.52
TT shape	–	0.01 - 0.01
W normalization	–	0.25 - 0.49
W shape	–	1.61 - 8.69
Z normalization	–	0.57 - 1.41
Z shape	–	0.01 - 0.01
Diboson shape	–	0.52 - 8.44
Total syst unc.	6.1 - 8.7	6.6 - 13.4
Total stat unc.	0.1 - 1.3	0.2 - 19.0

Table 2: Range of systematic uncertainties on the signal acceptance and background (BG) yields for the $\mu\nu$jj analysis. The last two lines show the total systematic uncertainty, and the total statistical uncertainty of the simulated samples, respectively.

widths determined by the number of events simulated in MC samples or observed in data control regions. These limits have been compared to so-called 'LHC-style' hybrid bayesian-frequentist CL_S limits [56] and are found to be in good agreement with the expected and observed limits for all final selections, but with slightly more conservative systematic uncertainties in the low background regime.

The 95% confidence level (CL) upper limits on $\sigma \times \beta^2$ or $\sigma \times 2\beta(1-\beta)$ as a function of LQ mass are shown together with the NLO predictions for the scalar LQ pair production cross section in Fig. 8. By comparing the observed upper limit with the theoretical cross section values, second-generation scalar LQs with masses less than 1530 (1150) GeV are excluded under the assumption that $\beta = 1$ (0.5). These numbers should be compared to the median expected limits of 1515 (1260) GeV.

Limits are set at 95% CL for β values from 0 to 1 for both the the $\mu\mu$jj and $\mu\nu$jj channels, as well as the combination of both channels. The combination of the two channels increases the sensitivity of the analysis, especially for small values of β. The resulting two-dimensional limit plot is shown in Fig. 9. The combination improves the mass exclusion for values of $\beta < 1$. Using the combined channels, second-generation scalar leptoquarks with masses less than 1285 GeV can be excluded for $\beta = 0.5$, compared with an expected limit of 1365 GeV.

Fig. 10 shows the 95% CL expected and observed limits on the displaced SUSY $\tilde{t}$ pair production cross section. The limits are presented in two dimensions as a function of $\tilde{t}$ mass (x axis) and lifetime (y axis). Extrapolation has been performed to produce a limit plot down to the prompt kinematic range. On the right hand side, the expected and observed limits have been extrapolated to the prompt LQ limits at $c\tau = 0$ cm, taking into account the different branching fractions to muons of the two models. This is motivated by the fact that prompt $\tilde{t}$s are kinematically very similar to LQs. The observed exclusion limits are 1150 GeV for $c\tau = 0.1$ cm, 940 GeV for $c\tau = 1.0$ cm, and 305 GeV for $c\tau = 10.0$ cm. These limits provide complimentary sensitivity to dedicated searches for long-lived particles.

7 Conclusion

A search has been performed for pair production of second-generation leptoquarks using 35.9 fb^{-1} of proton-proton collisions collected at $\sqrt{s}$=13 TeV in 2016 with the CMS detector at the CERN LHC. Limits have been set on pair production in the $\mu\mu$jj ($\mu\nu$jj) channels for $\beta = 1$ (0.5) as a function of leptoquark mass. Two-dimensional limits have also been set in the β – leptoquark mass plane. The $\mu\mu$jj search has been reinterpreted in the context of a displaced SUSY model. These limits represent the most stringent limits to date on these models.

Acknowledgments

We congratulate our colleagues in the CERN accelerator departments for the excellent performance of the LHC and thank the technical and administrative staffs at CERN and at other CMS institutes for their contributions to the success of the CMS effort. In addition, we gratefully acknowledge the computing centers and personnel of the Worldwide LHC Computing Grid for delivering so effectively the computing infrastructure essential to our analyses. Finally, we acknowledge the enduring support for the construction and operation of the LHC and the CMS detector provided by the following funding agencies: BMWFW and FWF (Austria); FNRS and FWO (Belgium); CNPq, CAPES, FAPERJ, and FAPESP (Brazil); MES (Bulgaria); CERN; CAS, MoST, and NSFC (China); COLCIENCIAS (Colombia); MSES and CSF (Croatia);

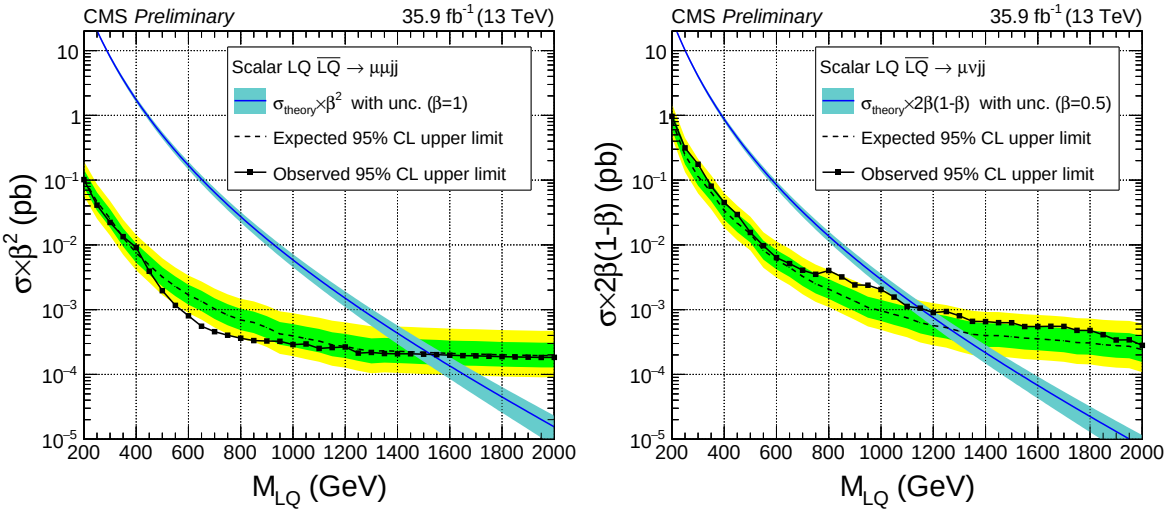

Figure 8: The expected and observed upper limits at 95% CL on the leptoquark pair production cross section times β^2 ($2\beta(1-\beta)$) as a function of the second-generation leptoquark mass obtained with the $\mu\mu jj$ (left) and $\mu\nu jj$ (right) analysis. The solid lines represent the observed limits, the dashed lines represent the median expected limits, and the colored bands represent the 68% and 95% confidence intervals. The σ_{theory} curves and their bands represent, respectively, the theoretical scalar leptoquark pair production cross section and the uncertainties due to the choice of PDF and renormalization/factorization scales.

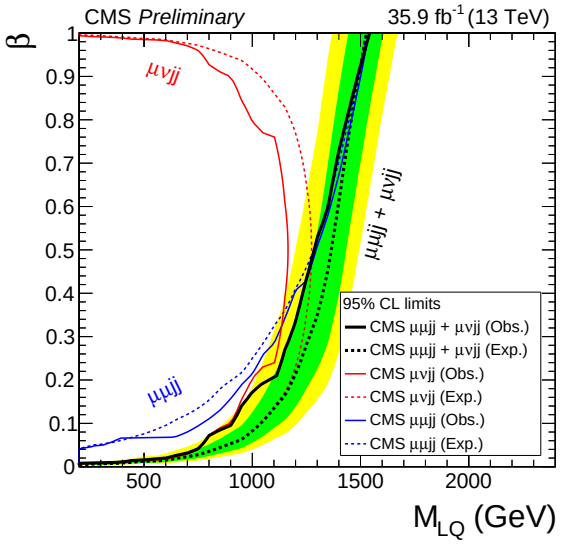

Figure 9: The expected and observed exclusion limits at 95% CL for second-generation leptoquark mass as a function of the branching fraction β vs. LQ mass M_{LQ}. The dark green and light yellow expected limit uncertainty bands represent the 68% and 95% confidence intervals on the combination. Limits for the individual $\mu\mu jj$ and $\mu\nu jj$ channels are also given. Solid lines represent the observed limits in each channel, and dashed lines represent the expected limits.

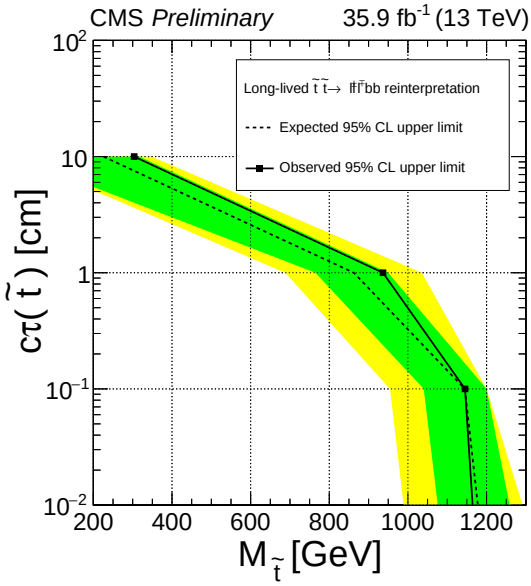

Figure 10: Expected and observed upper limits at 95% CL on the long-lived RPV SUSY $\tilde{t}$ pair production cross section as a function of $\tilde{t}$ mass (x-axis) and lifetime (y-axis). The expected limits and uncertainty bands represent the median expected limits and the 68% and 95% confidence intervals. Extrapolation has been performed to produce a limit plot down to the prompt kinematic range.

RPF (Cyprus); SENESCYT (Ecuador); MoER, ERC IUT, and ERDF (Estonia); Academy of Finland, MEC, and HIP (Finland); CEA and CNRS/IN2P3 (France); BMBF, DFG, and HGF (Germany); GSRT (Greece); OTKA and NIH (Hungary); DAE and DST (India); IPM (Iran); SFI (Ireland); INFN (Italy); MSIP and NRF (Republic of Korea); LAS (Lithuania); MOE and UM (Malaysia); BUAP, CINVESTAV, CONACYT, LNS, SEP, and UASLP-FAI (Mexico); MBIE (New Zealand); PAEC (Pakistan); MSHE and NSC (Poland); FCT (Portugal); JINR (Dubna); MON, RosAtom, RAS, RFBR and RAEP (Russia); MESTD (Serbia); SEIDI, CPAN, PCTI and FEDER (Spain); Swiss Funding Agencies (Switzerland); MST (Taipei); ThEPCenter, IPST, STAR, and NSTDA (Thailand); TUBITAK and TAEK (Turkey); NASU and SFFR (Ukraine); STFC (United Kingdom); DOE and NSF (USA).

References

[1] J. C. Pati and A. Salam, "Unified lepton-hadron symmetry and a gauge theory of the basic interactions", *Phys. Rev. D* **8** (1973) 1240, doi:10.1103/PhysRevD.8.1240.

[2] J. C. Pati and A. Salam, "Lepton number as the fourth color", *Phys. Rev. D* **10** (1974) 275, doi:10.1103/PhysRevD.10.275.

[3] H. Georgi and S. Glashow, "Unity of all elementary-particle forces", *Phys. Rev. Lett.* **32** (1974) 438, doi:10.1103/PhysRevLett.32.438.

[4] H. Murayama and T. Yanagida, "A viable SU(5) GUT with light leptoquark bosons", *Mod. Phys. Lett. A* **7** (1992) 147, doi:10.1142/S0217732392000070.

[5] H. Fritzsch and P. Minkowski, "United interactions of leptons and hadrons", *Annals Phys.* **93** (1975) 193, doi:10.1016/0003-4916(75)90211-0.

[6] G. Senjanović and A. Sokorac, "Light lepto-quarks in SO(10)", *Z. Phys. C* **20** (1983) 255, doi:10.1007/BF01574858.

[7] P. H. Frampton and B.-H. Lee, "SU(15) Grand Unification", *Phys. Rev. Lett.* **64** (1990) 619, doi:10.1103/PhysRevLett.64.619.

[8] P. H. Frampton and T. W. Kephart, "Higgs Sector and Proton Decay in SU(15q) Grand Unification", *Phys. Rev. D* **42** (1990) 3892, doi:10.1103/PhysRevD.42.3892.

[9] B. Schrempp and F. Schrempp, "Light leptoquarks", *Phys. Lett. B* **153** (1985) 101, doi:10.1016/0370-2693(85)91450-9.

[10] S. Dimopoulos and L. Susskind, "Mass without scalars", *Nucl. Phys. B* **155** (1979) 237, doi:10.1016/0550-3213(81)90304-7.

[11] S. Dimopoulos, "Technicolored signatures", *Nucl. Phys. B* **168** (1980) 69, doi:10.1016/0550-3213(80)90277-1.

[12] E. Eichten and K. Lane, "Dynamical breaking of the weak interaction symmetries", *Phys. Lett. B* **90** (1980) 85, doi:10.1016/0370-2693(80)90065-9.

[13] J. L. Hewett and T. G. Rizzo, "Low-energy phenomenology of superstring-inspired E_6 models", *Phys. Lett.* **183** (1989) 193, doi:10.1016/0370-1573(89)90071-9.

[14] Belle Collaboration, "Observation of B0→D*- $\tau^+\nu_\tau$ decay at Belle", *Phys. Rev. Lett.* **99** (2007) 191807, doi:10.1103/PhysRevLett.99.191807, arXiv:0706.4429.

[15] Belle Collaboration, "Observation of $B^+ \to \overline{D}^*0\tau^+\nu_\tau$ and Evidence for $B^+ \to \overline{D}^0\tau^+\nu_\tau$ at Belle", *Phys. Rev.* **D82** (2010) 072005, doi:10.1103/PhysRevD.82.072005, arXiv:1005.2302.

[16] Belle Collaboration, "Measurement of the branching ratio of $\bar{B} \to D^{(*)}\tau^-\bar{\nu}_\tau$ relative to $\bar{B} \to D^{(*)}\ell^-\bar{\nu}_\ell$ decays with hadronic tagging at Belle", *Phys. Rev.* **D92** (2015), no. 7, 072014, doi:10.1103/PhysRevD.92.072014, arXiv:1507.03233.

[17] BaBar Collaboration, "Evidence for an excess of $\bar{B} \to D^{(*)}\tau^-\bar{\nu}_\tau$ decays", *Phys. Rev. Lett.* **109** (2012) 101802, doi:10.1103/PhysRevLett.109.101802, arXiv:1205.5442.

[18] BaBar Collaboration, "Measurement of an Excess of $\bar{B} \to D^{(*)}\tau^-\bar{\nu}_\tau$ Decays and Implications for Charged Higgs Bosons", *Phys. Rev.* **D88** (2013), no. 7, 072012, doi:10.1103/PhysRevD.88.072012, arXiv:1303.0571.

[19] LHCb Collaboration, "Measurement of the ratio of branching fractions $\mathcal{B}(\bar{B}^0 \to D^{*+}\tau^-\bar{\nu}_\tau)/\mathcal{B}(\bar{B}^0 \to D^{*+}\mu^-\bar{\nu}_\mu)$", *Phys. Rev. Lett.* **115** (2015), no. 11, 111803, doi:10.1103/PhysRevLett.115.159901, 10.1103/PhysRevLett.115.111803, arXiv:1506.08614. [Erratum: Phys. Rev. Lett.115,no.15,159901(2015)].

[20] LHCb Collaboration, "Measurement of Form-Factor-Independent Observables in the Decay $B^0 \to K^{*0}\mu^+\mu^-$", *Phys. Rev. Lett.* **111** (2013) 191801, doi:10.1103/PhysRevLett.111.191801, arXiv:1308.1707.

[21] LHCb Collaboration, "Test of lepton universality using $B^+ \to K^+\ell^+\ell^-$ decays", *Phys. Rev. Lett.* **113** (2014) 151601, doi:10.1103/PhysRevLett.113.151601, arXiv:1406.6482.

[22] H. K. Dreiner, "An introduction to explicit *R*-parity violation", *Pramana* **51** (1998) 123, doi:10.1007/BF02827485.

[23] P. W. Graham, D. E. Kaplan, S. Rajendran, and P. Saraswat, "Displaced supersymmetry", *Journal of High Energy Physics* **2012** (2012), no. 7, 1, doi:10.1007/JHEP07(2012)149.

[24] CMS Collaboration, "The cms experiment at the cern lhc", *JINST* **3** (2008) S08004, doi:doi:10.1088/1748-0221/3/08/S08004.

[25] CMS Collaboration, "CMS Luminosity Measurement for the 2015 Data Taking Period", *CMS Physics Analysis Summary: LUM-15-001* (2016).

[26] NNPDF Collaboration, "Parton distributions for the LHC Run II", *JHEP* **04** (2015) 040, doi:10.1007/JHEP04(2015)040, arXiv:1410.8849.

[27] GEANT4 Collaboration, "GEANT4: A simulation toolkit", *Nucl. Instrum. Meth.* **A506** (2003) 250–303, doi:10.1016/S0168-9002(03)01368-8.

[28] J. Allison et al., "Geant4 developments and applications", *IEEE Trans. Nucl. Sci.* **53** (2006) 270, doi:10.1109/TNS.2006.869826.

[29] T. Sjöstrand et al., "High-energy-physics event generation with pythia6.1", *Comp. Phys. Comm.* **135** (2001) 238, doi:10.1016/S0010-4655(00)00236-8.

[30] T. Sjöstrand, S. Mrenna, and P. Z. Skands, "A Brief Introduction to PYTHIA 8.1", *Comput. Phys. Commun.* **178** (2008) 852, doi:10.1016/j.cpc.2008.01.036, arXiv:0710.3820.

[31] J. Pumplin et al., "New generation of parton distributions with uncertainties from global QCD analysis", *JHEP* **07** (2002) 012, doi:10.1088/1126-6708/2002/07/012.

[32] W. Beenakker et al., "Stop production at hadron colliders", *Nucl. Phys. B* **515** (1998) 3, doi:10.1016/S0550-3213(98)00014-5, arXiv:hep-ph/9710451.

[33] W. Beenakker et al., "Supersymmetric top and bottom squark production at hadron colliders", *JHEP* **08** (2010) 098, doi:10.1007/JHEP08(2010)098, arXiv:1006.4771.

[34] W. Beenakker et al., "Squark and Gluino Hadroproduction", *Int. J. Mod. Phys. A* **26** (2011) 2637, doi:10.1142/S0217751X11053560, arXiv:1105.1110.

[35] J. Alwall et al., "The automated computation of tree-level and next-to-leading order differential cross sections, and their matching to parton shower simulations", *JHEP* **07** (2014) 079, doi:10.1007/JHEP07(2014)079, arXiv:1405.0301.

[36] S. Frixione and B. R. Webber, "Matching NLO QCD computations and parton shower simulations", *JHEP* **06** (2002) 029, doi:10.1088/1126-6708/2002/06/029, arXiv:hep-ph/0204244.

[37] S. Frixione, P. Nason, and C. Oleari, "Matching NLO QCD computations with parton shower simulations: the POWHEG method", *JHEP* **11** (2007) 070, doi:10.1088/1126-6708/2007/11/070, arXiv:0709.2092.

[38] S. Alioli, P. Nason, C. Oleari, and E. Re, "A general framework for implementing NLO calculations in shower Monte Carlo programs: the POWHEG BOX", *JHEP* **06** (2010) 043, doi:10.1007/JHEP06(2010)043, arXiv:1002.2581.

[39] S. Alioli, P. Nason, C. Oleari, and E. Re, "NLO vector-boson production matched with shower in POWHEG", *JHEP* **07** (2008) 060, doi:10.1088/1126-6708/2008/07/060.

[40] R. Gavin, Y. Li, F. Petriello, S. Quackenbush, "FEWZ 2.0: A code for hadronic Z production at next-to-next-to-leading order", arXiv:1011.3540.

[41] J. Campbell, R. K. Ellis, and F. Tramontano, "Single top-quark production and decay at next-to-leading order", *Phys. Rev. D* **70** (2004) 094012, doi:10.1103/PhysRevD.70.094012, arXiv:hep-ph/0408158.

[42] J. Campbell and F. Tramontano, "Next-to-leading order corrections to Wt production and decay", *Nucl. Phys. B* **726** (2005) 109, doi:10.1016/j.nuclphysb.2005.08.015, arXiv:hep-ph/0506289.

[43] J. M. Campbell, R. Frederix, F. Maltoni, and F. Tramontano, "Next-to-leading-order predictions for *t*-channel single-top production at hadron colliders", *Phys. Rev. Lett.* **102** (2009) 182003, doi:10.1103/PhysRevLett.102.182003, arXiv:0903.0005.

[44] J. M. Campbell, R. K. Ellis, and C. Williams, "Vector boson pair production at the LHC", *JHEP* **07** (2011) 018, doi:10.1007/JHEP07(2011)018, arXiv:1105.0020.

[45] M. Czakon, P. Fiedler, and A. Mitov, "The total top quark pair production cross-section at hadron colliders through $O(\alpha_S^4)$", *Phys. Rev. Lett.* **110** (2013) 252004, doi:10.1103/PhysRevLett.110.252004, arXiv:1303.6254.

[46] M. Czakon, M. L. Mangano, A. Mitov, and J. Rojo, "Constraints on the gluon PDF from top quark pair production at hadron colliders", *JHEP* **07** (2013) 167, doi:10.1007/JHEP07(2013)167, arXiv:1303.7215.

[47] CMS Collaboration, "Particle-flow reconstruction and global event description with the cms detector", *JINST* **12** (2017) P10003, doi:10.1088/1748-0221/12/10/P10003, arXiv:1706.04965.

[48] M. Cacciari, G. P. Salam, and G. Soyez, "The anti-kt jet clustering algorithm", *JHEP* **2008** (2008) 063, doi:10.1088/1126-6708/2008/04/063.

[49] M. Cacciari, G. P. Salam, and G. Soyez, "FastJet user manual", *Eur. Phys. J. C* **72** (2012) 1896, doi:10.1140/epjc/s10052-012-1896-2, arXiv:1111.6097.

[50] CMS Collaboration, "Performance of CMS muon reconstruction in pp collision events at $\sqrt{s} = 7$ TeV", *JINST* **7** (2012) 10002, doi:10.1088/1748-0221/7/10/P10002, arXiv:1206.4071.

[51] CMS Collaboration, "Performance of electron reconstruction and selection with the CMS detector in proton-proton collisions at $\sqrt{s} = 8$ TeV", *JINST* **10** (2015) P06005, doi:10.1088/1748-0221/10/06/P06005, arXiv:1502.02701.

[52] G. Punzi, "Sensitivity of searches for new signals and its optimization", *eConf* **C030908** (2003) MODT002, arXiv:physics/0308063. [,79(2003)].

[53] CMS Collaboration, "Identification of heavy-flavour jets with the CMS detector in pp collisions at 13 TeV", (2017). arXiv:1712.07158. Submitted to *JINST*.

[54] T. Junk, "Confidence level computation for combining searches with small statistics", *Nucl.Instrum.Meth.* **A434** (1999) 435, doi:10.1016/S0168-9002(99)00498-2, arXiv:hep-ex/9902006.

[55] A. L. Read, "Modified frequentist analysis of search results (the CL_s method)", *CERN-OPEN-2000-205* (2000) doi:10.5170/CERN-2000-005.81.

[56] ATLAS and CMS Collaborations, "Procedure for the LHC Higgs boson search combination in summer 2011", Technical Report CMS-NOTE-2011-005, ATL-PHYS-PUB-2011-11, 2011.

A Supplemental information

B Supplemental Material

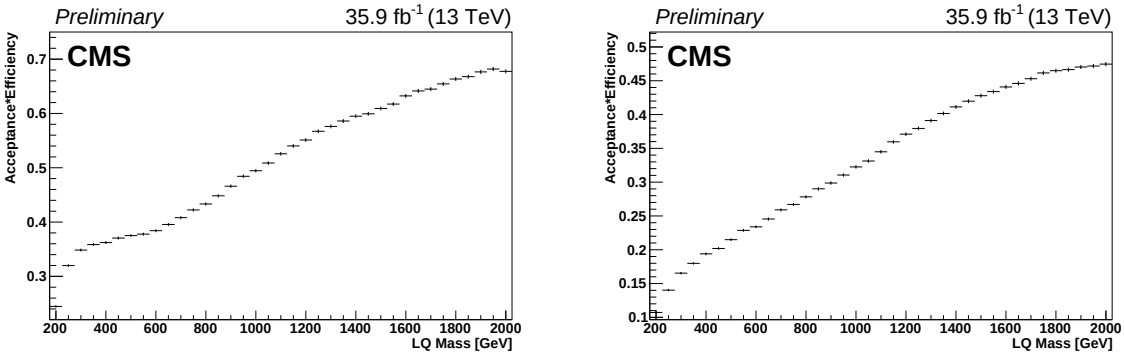

Figure 11: Signal acceptance*efficiency for optimized final selections as a function of scalar LQ mass in the $\mu\mu$jj (left) and $\mu\nu$jj (right) channels.

M_{LQ}	Signal	Z+Jets	$t\bar{t}$	VV	Other BG	All BG (stat + syst)	Data
200	531700 ± 4700	2973.2 ± 7.4	5467 ± 56	369 ± 2.0	519.4 ± 9.6	$9328 \pm 57 \pm 444$	9317
250	232900 ± 1800	1675 ± 5.1	2972 ± 41	241.5 ± 1.7	324.6 ± 7.5	$5213 \pm 42 \pm 250$	5102
300	100460 ± 760	792.9 ± 3.0	1298 ± 26	138.9 ± 1.3	189.2 ± 5.7	$2419 \pm 27 \pm 117$	2360
350	46160 ± 340	387.9 ± 1.8	538 ± 16	81.1 ± 1.0	98 ± 4.1	$1105 \pm 17 \pm 57$	1113
400	22610 ± 160	202.4 ± 1.2	237 ± 10	51.89 ± 0.84	55.2 ± 3.1	$546 \pm 11 \pm 29$	572
450	12039 ± 86	131.72 ± 0.92	120.7 ± 7.2	32.19 ± 0.66	31.8 ± 2.3	$316.4 \pm 7.7 \pm 18.2$	299
500	6672 ± 48	79 ± 0.65	54.1 ± 4.6	20.92 ± 0.53	20.2 ± 1.9	$174.2 \pm 5.0 \pm 11.1$	147
550	3848 ± 27	51.95 ± 0.5	26.1 ± 3.0	14.43 ± 0.46	13.1 ± 1.5	$105.6 \pm 3.4 \pm 7.6$	78
600	2328 ± 16	34.71 ± 0.39	12.9 ± 1.9	10.05 ± 0.38	9.44 ± 1.29	$67.1 \pm 2.4 \pm 5.2$	44
650	1461 ± 10	26.03 ± 0.33	9.9 ± 1.8	6.55 ± 0.3	6.7 ± 1.1	$49.1 \pm 2.1 \pm 3.9$	26
700	948.4 ± 6.5	18.19 ± 0.26	4.68 ± 1.07	4.36 ± 0.24	4.53 ± 0.91	$31.8 \pm 1.4 \pm 2.6$	16
750	630.1 ± 4.2	12.36 ± 0.19	3.47 ± 0.93	3.17 ± 0.2	3.04 ± 0.74	$22 \pm 1.2 \pm 1.9$	11
800	424.2 ± 2.8	9.18 ± 0.16	2.62 ± 0.83	2.45 ± 0.19	2.26 ± 0.63	$16.5 \pm 1.1 \pm 1.6$	8
850	292.7 ± 1.9	6.93 ± 0.13	3.89 ± 1.23	1.88 ± 0.17	2.05 ± 0.6	$14.8 \pm 1.4 \pm 1.1$	7
900	205.6 ± 1.3	5.55 ± 0.11	2.34 ± 0.88	1.44 ± 0.15	1.49 ± 0.5	$10.82 \pm 1.03 \pm 0.89$	6
950	146.75 ± 0.92	4.405 ± 0.097	0.22 ± 0.13	1.31 ± 0.15	1.105 ± 0.425	$7.04 \pm 0.48 \pm 0.71$	5
1000	103.92 ± 0.65	3.663 ± 0.087	0.72 ± 0.42	1.1 ± 0.13	0.733 ± 0.334	$6.21 \pm 0.56 \pm 0.59$	4
1050	74.98 ± 0.46	3.234 ± 0.083	0.466 ± 0.33	0.93 ± 0.12	0.603 ± 0.311	$5.24 \pm 0.48 \pm 0.56$	4
1100	54.86 ± 0.33	2.712 ± 0.074	0.602 ± 0.426	0.69 ± 0.1	0.603 ± 0.311	$4.6 \pm 0.54 \pm 0.48$	3
1150	40.3 ± 0.24	2.39 ± 0.069	0.036 ± 0.036	0.69 ± 0.1	0.412 ± 0.246	$3.53 \pm 0.28 \pm 0.42$	3
1200	29.65 ± 0.17	1.859 ± 0.058	0.193 ± 0.193	0.63 ± 0.1	0.412 ± 0.246	$3.1 \pm 0.33 \pm 0.42$	3
1250	22.17 ± 0.13	1.675 ± 0.055	0.223 ± 0.223	0.559 ± 0.099	0.198 ± 0.188	$2.65 \pm 0.31 \pm 0.34$	2
1300	16.425 ± 0.095	1.129 ± 0.04	0.299 ± 0.299	0.53 ± 0.1	0.198 ± 0.188	$2.15 \pm 0.37 \pm 0.27$	2
1350	12.296 ± 0.07	1.261 ± 0.047	0.46 ± 0.46	0.53 ± 0.1	0.198 ± 0.188	$2.45 \pm 0.51 \pm 0.24$	2
1400	9.238 ± 0.052	1.144 ± 0.044	0.544 ± 0.544	0.54 ± 0.11	$0.188^{+0.279}_{-0.188}$	$2.41^{+0.62}_{-0.59} \pm 0.24$	2
1450	6.899 ± 0.039	1.057 ± 0.044	0.575 ± 0.575	0.5 ± 0.11	$0.188^{+0.279}_{-0.188}$	$2.32^{+0.65}_{-0.62} \pm 0.22$	2
1500	5.243 ± 0.029	1.054 ± 0.045	0.588 ± 0.588	0.47 ± 0.11	$0.188^{+0.279}_{-0.188}$	$2.3^{+0.66}_{-0.63} \pm 0.23$	2
1550	3.985 ± 0.022	1.054 ± 0.045	0.588 ± 0.588	0.47 ± 0.11	$0.188^{+0.279}_{-0.188}$	$2.3^{+0.66}_{-0.63} \pm 0.23$	2
1600	3.062 ± 0.017	1.054 ± 0.045	0.588 ± 0.588	0.47 ± 0.11	$0.188^{+0.279}_{-0.188}$	$2.3^{+0.66}_{-0.63} \pm 0.23$	2
1650	2.346 ± 0.013	1.054 ± 0.045	0.588 ± 0.588	0.47 ± 0.11	$0.188^{+0.279}_{-0.188}$	$2.3^{+0.66}_{-0.63} \pm 0.23$	2
1700	1.7899 ± 0.0097	1.054 ± 0.045	0.588 ± 0.588	0.47 ± 0.11	$0.188^{+0.279}_{-0.188}$	$2.3^{+0.66}_{-0.63} \pm 0.23$	2
1750	1.3801 ± 0.0075	1.054 ± 0.045	0.588 ± 0.588	0.47 ± 0.11	$0.188^{+0.279}_{-0.188}$	$2.3^{+0.66}_{-0.63} \pm 0.23$	2
1800	1.0659 ± 0.0057	1.054 ± 0.045	0.588 ± 0.588	0.47 ± 0.11	$0.188^{+0.279}_{-0.188}$	$2.3^{+0.66}_{-0.63} \pm 0.23$	2
1850	0.821 ± 0.004	1.054 ± 0.045	0.588 ± 0.588	0.47 ± 0.11	$0.188^{+0.279}_{-0.188}$	$2.3^{+0.66}_{-0.63} \pm 0.23$	2
1900	0.636 ± 0.003	1.054 ± 0.045	0.588 ± 0.588	0.47 ± 0.11	$0.188^{+0.279}_{-0.188}$	$2.3^{+0.66}_{-0.63} \pm 0.23$	2
1950	0.491 ± 0.003	1.054 ± 0.045	0.588 ± 0.588	0.47 ± 0.11	$0.188^{+0.279}_{-0.188}$	$2.3^{+0.66}_{-0.63} \pm 0.23$	2
2000	0.377 ± 0.002	1.054 ± 0.045	0.588 ± 0.588	0.47 ± 0.11	$0.188^{+0.279}_{-0.188}$	$2.3^{+0.66}_{-0.63} \pm 0.23$	2

Table 3: Event yields at final selection level for the $\mu\mu jj$ analysis. 'Other BG' includes W+jets and single top. Uncertainties are statistical unless otherwise indicated.

M_{LQ}	Signal	W+Jets	$t\bar{t}$	VV	Other BG	All BG (stat + syst)	Data
200	116600 ± 1500	5672 ± 26	15816 ± 51	1049.6 ± 5.0	2732 ± 15	$25270 \pm 59 \pm 1171$	26043
250	51050 ± 580	2635 ± 16	4662 ± 28	575.9 ± 3.7	1155 ± 10	$9029 \pm 34 \pm 431$	9519
300	23840 ± 250	1259.2 ± 9.7	2066 ± 18	346.8 ± 3.0	611.7 ± 7.6	$4284 \pm 22 \pm 197$	4669
350	11580 ± 120	757.1 ± 7.2	964 ± 13	200.7 ± 2.3	335 ± 5.6	$2256 \pm 16 \pm 122$	2379
400	6051 ± 58	418.2 ± 4.8	461.3 ± 8.8	131.5 ± 1.9	176 ± 4.2	$1187 \pm 11 \pm 70$	1279
450	3280 ± 32	248.1 ± 3.4	228.4 ± 6.2	86.4 ± 1.6	108.1 ± 3.4	$671 \pm 8.0 \pm 47$	737
500	1911 ± 18	177.2 ± 2.8	119.3 ± 4.4	58.8 ± 1.3	67.6 ± 2.7	$422.9 \pm 6.1 \pm 40$	430
550	1165 ± 10	99.2 ± 1.8	69.2 ± 3.4	44 ± 1.2	42.9 ± 2.1	$255.4 \pm 4.6 \pm 18.9$	270
600	708.9 ± 6.2	70.9 ± 1.5	43.4 ± 2.7	31.1 ± 1.0	28.6 ± 1.7	$174 \pm 3.7 \pm 13$	179
650	453.4 ± 3.9	53.8 ± 1.3	26.8 ± 2.1	22.89 ± 0.91	19.7 ± 1.4	$123.2 \pm 3.0 \pm 10.1$	130
700	301 ± 2.5	36.02 ± 0.96	16.7 ± 1.7	17.03 ± 0.78	14.8 ± 1.2	$84.6 \pm 2.4 \pm 7.1$	93
750	199.2 ± 1.6	22.73 ± 0.68	11.59 ± 1.43	13.32 ± 0.71	9.89 ± 0.96	$57.5 \pm 2.0 \pm 5.2$	68
800	136.2 ± 1.1	13.95 ± 0.46	7.6 ± 1.15	8.58 ± 0.52	7.6 ± 0.83	$37.7 \pm 1.6 \pm 4.3$	57
850	94.69 ± 0.75	10.49 ± 0.37	4.88 ± 0.92	7.46 ± 0.52	6.51 ± 0.81	$29.3 \pm 1.4 \pm 3.5$	45
900	65.88 ± 0.51	8.96 ± 0.34	3.43 ± 0.79	6.14 ± 0.48	5.56 ± 0.75	$24.1 \pm 1.2 \pm 2.4$	35
950	47.05 ± 0.36	5.96 ± 0.25	2.36 ± 0.65	4.85 ± 0.42	3.7 ± 0.55	$16.87 \pm 0.99 \pm 1.69$	30
1000	33.89 ± 0.25	5.4 ± 0.24	1.66 ± 0.55	4.3 ± 0.41	3.3 ± 0.52	$14.67 \pm 0.9 \pm 1.51$	26
1050	24.42 ± 0.18	4.2 ± 0.2	1.48 ± 0.52	3.9 ± 0.4	2.54 ± 0.45	$12.12 \pm 0.83 \pm 1.27$	20
1100	18 ± 0.13	4.16 ± 0.22	1.29 ± 0.49	3.31 ± 0.38	1.83 ± 0.33	$10.59 \pm 0.74 \pm 1.15$	15
1150	13.413 ± 0.095	3.05 ± 0.17	0.759 ± 0.379	2.87 ± 0.35	1.29 ± 0.28	$7.97 \pm 0.61 \pm 0.92$	13
1200	9.979 ± 0.07	3.02 ± 0.18	0.559 ± 0.323	2.29 ± 0.31	1.09 ± 0.23	$6.96 \pm 0.54 \pm 0.81$	11
1250	7.417 ± 0.052	2.68 ± 0.17	0.74 ± 0.37	2.07 ± 0.3	0.591 ± 0.137	$6.08 \pm 0.52 \pm 0.72$	11
1300	5.575 ± 0.038	1.61 ± 0.11	0.74 ± 0.37	1.79 ± 0.28	0.73 ± 0.14	$4.87 \pm 0.49 \pm 0.55$	9
1350	4.213 ± 0.028	1.026 ± 0.074	0.74 ± 0.37	1.5 ± 0.25	0.7 ± 0.14	$3.97 \pm 0.48 \pm 0.43$	7
1400	3.194 ± 0.022	1.005 ± 0.077	0.74 ± 0.37	1.33 ± 0.26	0.69 ± 0.14	$3.76 \pm 0.48 \pm 0.39$	7
1450	2.416 ± 0.016	1.45 ± 0.12	0.559 ± 0.323	1.32 ± 0.26	0.65 ± 0.14	$3.97 \pm 0.45 \pm 0.44$	7
1500	1.841 ± 0.012	1.29 ± 0.11	0.559 ± 0.323	1.32 ± 0.26	0.584 ± 0.138	$3.75 \pm 0.45 \pm 0.41$	7
1550	1.4007 ± 0.0091	1.12 ± 0.1	0.559 ± 0.323	1.32 ± 0.26	0.491 ± 0.137	$3.49 \pm 0.45 \pm 0.39$	6
1600	1.0671 ± 0.0069	1.07 ± 0.1	0.559 ± 0.323	1.27 ± 0.26	0.457 ± 0.137	$3.35 \pm 0.45 \pm 0.37$	6
1650	0.8159 ± 0.0053	0.884 ± 0.09	0.559 ± 0.323	1.27 ± 0.26	0.442 ± 0.137	$3.15 \pm 0.44 \pm 0.35$	6
1700	0.629 ± 0.004	0.99 ± 0.11	0.559 ± 0.323	1.05 ± 0.24	0.416 ± 0.137	$3.01 \pm 0.44 \pm 0.32$	6
1750	0.487 ± 0.003	0.91 ± 0.11	0.381 ± 0.27	0.98 ± 0.23	0.384 ± 0.136	$2.65 \pm 0.39 \pm 0.3$	5
1800	0.373 ± 0.002	0.91 ± 0.11	0.381 ± 0.27	0.96 ± 0.24	0.359 ± 0.136	$2.61 \pm 0.4 \pm 0.29$	5
1850	0.287 ± 0.002	0.88 ± 0.11	0.199 ± 0.199	0.9 ± 0.23	0.321 ± 0.136	$2.3 \pm 0.35 \pm 0.28$	4
1900	0.221 ± 0.001	0.74 ± 0.097	0.199 ± 0.199	0.86 ± 0.24	0.309 ± 0.136	$2.11 \pm 0.35 \pm 0.25$	3
1950	0.17 ± 0.001	0.685 ± 0.096	0.199 ± 0.199	0.83 ± 0.24	0.3 ± 0.136	$2.02 \pm 0.35 \pm 0.24$	3
2000	0.132 ± 0.001	0.68 ± 0.1	0.199 ± 0.199	0.29 ± 0.088	0.295 ± 0.136	$1.47 \pm 0.28 \pm 0.15$	2

Table 4: Event yields at final selection level for the $\mu\nu jj$ analysis. 'Other BG' includes Z+jets and single top.Uncertainties are statistical unless otherwise indicated.